UNIVERSITY OF GOTHENBURG

QUANTITATIVE IMAGE RECOVERY FROM MEASURED BLIND BACKSCATTERED DATA USING A GLOBALLY CONVERGENT INVERSE METHOD

ANDREY V. KUZHUGET[1] , LARISA BEILINA[2] , MICHAEL V. KLIBANOV[3] , ANDERS SULLIVAN[4] , LAM NGUYEN[4] , AND MICHAEL A. FIDDY[5]

Abstract. The goal of this paper is to estimate dielectric constants of targets using time resolved backscattering data collected by a forward looking radar of the US Army Research Laboratory. Only blind experimental data are considered. This problem is formulated as a coefficient inverse problem for a 1D hyperbolic partial differential equation. That coefficient inverse problem is solved by a new algorithm. The main new feature of this algorithm is its rigorously established global convergence property. Calculated values of dielectric constants are in a good agreement with material properties, which were revealed a posteriori.

Index Terms—remote sensing, inverse scattering, quantitative imaging, blind experimental data

1. Introduction. A fundamental problem in remote sensing is the processing of scattered field data from strongly scattering, penetrable targets. Multiple scattering renders this problem extremely difficult to solve, it being ill-conditioned with additional questions of uniqueness and, the most difficult, non-linearity to contend with. In practice limited noisy data typically require that some physical model be assumed from which one hopes to extract meaningful and preferably quantitative information about the target in question. A number of recent publications by Beilina, Klibanov et. al. [3, 4, 5, 6, 7, 8, 12, 14, 15, 16] have led to a new approach to address this important topic. This numerical method was developed for some Multidimensional Coefficient Inverse Problems (MCIPs) for a hyperbolic Partial Differential Equation (PDE) using data from only a single location of either a point source or from a single direction of an incident plane wave. The 1D version of this method [14] is used here to work with the experimental data. The illuminating field is pulsed in time and the time history of the backscattering from the illuminated target volume constitutes the measured data, processed by this algorithm. The authors are unaware of other groups working on MCIPs using single measurement data. However, the single measurement case is clearly the most practical one, especially for military applications. Indeed, because of many dangers on the battlefield, the number of measurements should be minimized.

The new algorithm of above cited publications computes values for the spatial distribution of the dielectric constants of objects within the target volume. It is important to stress that this algorithm requires no prior knowledge of what might exist in the target volume nor a prior knowledge of a good first guess about the solution. There is a rigorous guarantee that this algorithm converges globally, see mathematical details in [7, 14, 16, 17]. Because of the global convergence property, estimates of spatially distributed dielectric constants are reliable and systematically improve with more measured data and less noisy data. The theory of above cited publications rigorously guarantees that this numerical method delivers a good approximation to the exact solution of an MCIP without any *a priori* information about a small neighborhood of the exact solution as long as iterations start from the so-called "first tail function" $V_0(x)$, which can be easily computed using available boundary measurements, see (2.27)-(2.29) in subsection 2.3. And it is in this sense that we use the term "global convergence" of the algorithm. The common perception of the term "global convergence" is that one can start from any point and still get the solution, but we stress that actually we start not from any point, but rather from the function $V_0(x)$, which can be easily computed from the

*[1]Morgan Stanley & Co. Incorporated, 1585 Broadway, New York, NY 10036, USA

[2]Department of Mathematical Sciences, Chalmers University of Technology and Gothenburg University, SE-42196 Gothenburg, Sweden, *email*: larisa@chalmers.se

[3]Corresponding author, Department of Mathematics and Statistics, University of North Carolina at Charlotte, Charlotte, NC 28223, USA, *email*: mklibanv@uncc.edu

[4] US Army Research Laboratory, 2800 Powder Mill Road Adelphy, MD 20783-1197, USA, *emails*: anders.j.sullivan.civ@mail.mil, lam.h.nguyen2.civ@mail.mil

[5]Optoelectronics Center, University of North Carolina at Charlotte, Charlotte, NC 28223, USA, *email*: mafiddy@uncc.edu

boundary data, see (2.27)-(2.29) in subsection 2.3 which follows.

It is well known that least squares functionals for MCIPs suffer from multiple local minima and ravines. Hence, local convergence of numerical methods to incorrect estimates will occur unless an initial guess is used that is close to the true solution. Such a guess is rarely available in applications. Unlike this, the algorithm of above cited publications, including the current paper, does not use a least squares functional. Therefore, it is free from the problem of local minima. Instead this algorithm relies on the structure of the differential operator of the wave-like PDE.

Prior to the work reported here, a major focus by ARL had been on the development of image processing techniques [19] that would improve the radar image, rather than through the application of inverse scattering methods. By incorporating more physics of the target-wave electromagnetic response into the data processing, one can greatly improve target detection and identification. Present data processing provides an electromagnetic field brightness or intensity map of the target volume which need not relate in a simple fashion to the scattering structures themselves. Our estimates of dielectric constants of targets obviously add an important new dimension to the interpretation of data acquired by this radar system, since specific bounds on the dielectric properties of a feature in the target volume can identify its likely material properties. Since no prior knowledge is required, the measured data were processed by Kuzhuget, Beilina, Klibanov and Fiddy in the most challenging "blind" scenario, i.e. without any knowledge of the actual target structures and their dielectric properties. Next, Sullivan and Nguyen compared *a posteriori* the image estimates with the actually known material characteristics.

The performance of this algorithm using experimental forward scattered data was reported previously, also in a blind experiment (see Tables 5 and 6 in [12] as well as Tables 5.5 and 5.6 in [7]). Images of [12] were further improved in the follow up publication [6] using the adaptivity technique of [1, 2, 4, 5, 7].

In section 2 we outline the basic steps in the underlying theory upon which the new algorithm is based. In section 3 we formulate the global convergence theorem. In section 4 we outline results obtained using time resolved backscatter electric field measurements collected in the field. Measurements were carried out by a forward looking radar system built and operated by the US Army Research Laboratory (ARL). The data were noisy, limited and the target volumes included miscellaneous sources of clutter. The purpose of this radar system is to detect and possibly identify shallow explosive-like targets.

2. Theoretical Background.

2.1. Integral differential equation. Since we were given only one time resolved experimental curve per target, we have no choice but to use a 1d mathematical model, although the reality is 3d, see section 3 for some details about the data collection. Also, since only one component of the electric wave field was both transmitted and measured, we have no choice but to model the process with one wave-like Partial Differential Equation rather than using complete Maxwell equations. We assume the constitutive parameter of interest, mapping the target volume, is a relative permittivity $\varepsilon_r(x)$. In other words we ignore magnetic effects in this paper. We also assume for convenience that $\varepsilon_r(x) = 1$ outside of the target volume, which is $x \in (0,1)$ in our case. We assume that the source $x_0 < 0$ lies outside of the target volume. In one spatial dimension, we can write the forward scattering problem as

$$\varepsilon_r(x) u_{tt} = u_{xx}, \ x \in \mathbb{R}, \tag{2.1}$$

$$u(x,0) = 0, u_t(x,0) = \delta(x - x_0). \tag{2.2}$$

The subscripts in (2.1) indicate the number of partial derivatives with respect to the variable indicated. The coefficient inverse problem (CIP) is to recover $\varepsilon_r(x)$ assuming that the initial illuminating pulse is known and that we measure the function $g(t)$,

$$u(0,t) = g(t) \tag{2.3}$$

for sufficiently large times t that all multiple scattering events within the target volume that can produce a measurable signal at the detector, do so. Practically we gate the radiation source in time and since the

2

Laplace Transform (LT), $w(x, s)$, is used to solve this CIP, the rapid decay $e^{-st}, s > 0$ of the LT kernel further limits the duration of the measured time history.

The LT is

$$w(x, s) = \int_0^\infty u(x, t) e^{-st} dt := \mathcal{L}u, \ s \geq \underline{s} = const. > 0, \tag{2.4}$$

and we assume that the so-called pseudo-frequency $s \geq s(\varepsilon_r(x)) := \underline{s}$, is sufficiently large. This gives [7]

$$w_{xx} - s^2 \varepsilon_r(x) w = -\delta(x - x_0), \ x \in \mathbb{R}, \tag{2.5}$$

$$\lim_{|x| \to \infty} w(x, s) = 0. \tag{2.6}$$

Let

$$w(0, s) = \varphi(s) = \mathcal{L}g. \tag{2.7}$$

be the LT of the measured function $g(t)$ in (2.3). Since $\varepsilon_r(x) = 1$ for $x < 0$, then, using (2.5), (2.6), one can prove that, in addition to the function $w(0, s)$ in (2.7), the function $w_x(0, s)$ is also known as (see [17])

$$w_x(0, s) = s\varphi(s) - \exp(sx_0). \tag{2.8}$$

Let $w_0(x, s)$ be the solution of the problem (2.5), (2.6) for the case of the uniform background $\varepsilon_r(x) \equiv 1$. Then

$$w_0(x, s) = \frac{\exp(-s|x - x_0|)}{2s}. \tag{2.9}$$

When implementing the algorithm, given the assumption of a uniform normalized $\varepsilon_r(x) = 1$ outside of the target volume, we consider the function

$$r(x, s) = \frac{1}{s^2} \ln\left(\frac{w}{w_0}(x, s)\right). \tag{2.10}$$

Since the source $x_0 < 0$, then the function $r(x, s)$ is the solution of the following equation in the interval $(0, 1)$

$$r_{xx} + s^2 r_x^2 - 2sr_x = \varepsilon_r(x) - 1, x \in (0, 1). \tag{2.11}$$

In addition, by (2.7) and (2.8)

$$r(0, s) = \varphi_0(s), r_x(0, s) = \varphi_1(s), \tag{2.12}$$

$$\varphi_0(s) = \frac{\ln \varphi(s) - \ln(2s)}{s^2} + \frac{x_0}{s}, \ \varphi_1(s) = \frac{2}{s} - \frac{e^{sx_0}}{s^2 \varphi(s)}. \tag{2.13}$$

The idea now is to eliminate the unknown coefficient $\varepsilon_r(x)$ from equation (2.11) via the differentiation with respect to the pseudo-frequency s. Differentiating (2.11) with respect to s and denoting $q(x, s) = \partial_s r(x, s)$, we obtain

$$q_{xx} + 2s^2 q_x r_x + 2sr_x^2 - 2sq_x - 2r_x = 0, x \in (0, 1). \tag{2.14}$$

3

We now need to express in (2.14) the function r via the function q. We have

$$r\left(x,s\right) = -\int_{s}^{\overline{s}} q\left(x,\tau\right) d\tau + V\left(x,\overline{s}\right), \tag{2.15}$$

where $V\left(x\right) := V\left(x,\overline{s}\right)$ is referred to as the *tail function*, which is small in practice for large positive $\overline{s}$. Here the truncation pseudo-frequency $\overline{s}$ serves as a regularization parameter. The exact formula for $V\left(x\right)$ is

$$V\left(x,\overline{s}\right) := V\left(x\right) = r\left(x,\overline{s}\right) = \frac{1}{\overline{s}^{2}} \ln\left(\frac{w\left(x,\overline{s}\right)}{w_{0}\left(x,\overline{s}\right)}\right). \tag{2.16}$$

Substituting (2.15) in (2.14), we obtain the following nonlinear integral differential equation

$$q_{xx} - 2s^{2}q_{x}\int_{s}^{\overline{s}} q_{x}\left(x,\tau\right) d\tau + 2s\left[\int_{s}^{\overline{s}} q_{x}\left(x,\tau\right) d\tau\right]^{2} - 2sq_{x} + 2\int_{s}^{\overline{s}} q_{x}\left(x,\tau\right) d\tau$$

$$+ 2s^{2}q_{x}V_{x} - 4sV_{x}\int_{s}^{\overline{s}} q_{x}\left(x,\tau\right) d\tau + 2s\left(V_{x}\right)^{2} - 2V_{x} = 0, \tag{2.17}$$

$$x \in \left(0,1\right), s \in \left[\underline{s},\overline{s}\right],$$

$$q\left(0,s\right) = \psi_{0}\left(s\right), q_{x}\left(0,s\right) = \psi_{1}\left(s\right), q_{x}\left(1,s\right) = 0, s \in \left[\underline{s},\overline{s}\right], \tag{2.18}$$

where functions $\psi_{0}\left(s\right) = \varphi_{0}'\left(s\right), \psi_{1}\left(s\right) = \varphi_{1}'\left(s\right)$ are derived from (2.13). The condition $q_{x}\left(1,s\right) = 0$ can be easily derived from (2.6) since $\varepsilon_{r}\left(x\right) = 1$ outside of the interval $\left(0,1\right)$.

In (2.17), (2.18) both functions $q\left(x,s\right)$ and $V\left(x\right)$ are unknown. The reason why we can approximate both of them is that we find updates for $q\left(x,s\right)$ via inner iterations exploring (2.17), (2.18) inside of the interval $\left(0,1\right)$. At the same time, we update the tail function $V\left(x\right)$ via outer iterations exploring the entire real line $\mathbb{R}$. In short, given an approximation for $V\left(x\right)$, the algorithm updates q and then updated for $\varepsilon_{r}\left(x\right)$. Next, the forward problem (2.5), (2.6) is solved for the function $w\left(x,s\right)$ for $s = \overline{s}$. Next, the tail function $V\left(x\right)$ is updated using (2.16). This might seem reminiscent of the steps in algorithms such as the modified gradient inverse scattering technique [20], but we emphasize that, unlike our case, such methods have no global convergence properties.

2.2. The iterative process. We now outline the formulation of our algorithm as well as the iterative process, see details in [7, 14, 16, 17]. Unlike computationally simulated data in [14], we do no use a knowledge of the function $q\left(1,s\right)$ on the transmitted edge, since this function is unknown to us. We have observed in our computational experiments that the knowledge of $q\left(1,s\right)$ affects only the accuracy of the calculation of the location of the target, but it does not affect the accuracy of the computed target/background contrast. At the same time, we are interested in this publication only in that contrast, see section 3. Since $\varepsilon_{r}\left(x\right) = 1$ for $x \geq 1$ and $x_{0} < 0$, then one can easily derive from equations (2.5), (2.9), (2.10) that $\partial_{x}q\left(1,s\right) = 0$.

Consider a partition of the interval $\left[\underline{s},\overline{s}\right]$ into N small subintervals with the small grid step size $h > 0$ and assume that the function $q\left(x,s\right)$ is piecewise constant with respect to s,

$$\underline{s} = s_{N} < s_{N-1} < ... < s_{0} = \overline{s}, s_{i-1} - s_{i} = h; \; q\left(x,s\right) = q_{n}\left(x\right), \text{ for } s \in \left(s_{n}, s_{n-1}\right]. \tag{2.19}$$

For each subinterval we $\left(s_{n}, s_{n-1}\right]$ we obtain a differential equation for the function $q_{n}\left(x\right)$. We assign for convenience of notations $q_{0} :\equiv 0$. Following the above idea of a combination of inner and outer iterations, we perform for each n inner iterations with respect to the tail function. This way we obtain functions $q_{n,k}, V_{n,k}$. The equation for the pair $\left(q_{n,k}, V_{n,k}\right)$ is

$$q_{n,k}'' - \left(A_{1,n}h \sum_{j=0}^{n-1} q_j' - A_{1,n}V_{n,k}' - 2A_{2,n} \right) q_{n,k}' =$$

$$-A_{2,n}h^2 \left(\sum_{j=0}^{n-1} q_j' \right)^2 + 2h \sum_{j=0}^{n-1} q_j' + 2A_{2,n}V_{n,k}' \left(h \sum_{j=0}^{n-1} q_j' \right) \qquad (2.20)$$

$$-A_{2,n} \left(V_{n,k}' \right)^2 + 2A_{2,n}V_{n,k}', \ x \in (0,1),$$

$$q_{n,k}(0) = \psi_{0,n}, \ q_{n,k}'(0) = \psi_{1,n}, \ q_{n,k}'(1) = 0, \qquad (2.21)$$

$$\psi_{0,n} = \frac{1}{h} \int_{s_n}^{s_{n-1}} \psi_0(s) \, ds, \ \psi_{1,n} = \frac{1}{h} \int_{s_n}^{s_{n-1}} \psi_1(s) \, ds.$$

Here $A_{1,n}, A_{2,n}$ are certain numbers, whose exact expression is given in [3, 7].

The choice of the first tail function $V_0(x)$ is described in subsection 2.3. Let $n \geq 1$. Suppose that for $j = 0,...n-1$ functions $q_j(x), V_j(x)$ are constructed already. We now need to construct functions $q_{n,k}, V_{n,k}$ for $k = 1,...,m$. We set $V_{n,1}(x) := V_{n-1}(x)$. Next, using the Quasi-Reversibility Method (QRM, subsection 2.3), we approximately solve equation (2.20) for $k = 1$ with over-determined boundary conditions (2.21) and find the function $q_{n,1}$. Next, we find the approximation $\varepsilon_r^{(n,1)}$ for the unknown coefficient $\varepsilon_r(x)$ via the following two formulas

$$r_{n,1}(x) = -hq_{n,1} - h \sum_{j=0}^{n-1} q_j + V_{n,1}, \ x \in [0,1], \qquad (2.22)$$

$$\varepsilon_r^{(n,1)}(x) = 1 + r_{n,1}''(x) + s_n^2 \left[r_{n,1}'(x) \right]^2 - 2s_n r_{n,1}'(x), \ x \in [0,1]. \qquad (2.23)$$

Next, we solve the forward problem (2.5), (2.6) with $\varepsilon_r(x) := \varepsilon_r^{(n,1)}(x), s := \overline{s}$ and find the function $w_{n,1}(x,\overline{s})$ this way. After this we update the tail via formula (2.16) in which $w(x,\overline{s}) := w_{n,1}(x,\overline{s})$. This way we obtain a new tail $V_{n,2}(x)$. Similarly we continue iterating with respect to tails m times. Next, we set

$$q_n(x) := q_{n,m}(x), \ V_n(x) := V_{n,m}(x), \ \varepsilon_r^{(n)}(x) := \varepsilon_r^{(n,m)}(x)$$

replace n with $n+1$ and repeat this process. We continue this process until [15]

$$\text{either } \left\| \varepsilon_r^{(n)} - \varepsilon_r^{(n-1)} \right\|_{L_2(0,1)} \leq 10^{-5} \text{ or } \|\nabla J_\alpha(q_{n,k})\|_{L_2(0,1)} \geq 10^{-5}, \qquad (2.24)$$

where the functional $J_\alpha(q_{n,k})$ is defined in subsection 2.3. Here the norm in the space $L_2(0,1)$ is understood in the discrete sense. In the case when the second inequality (2.24) is satisfied, we stop at the previous iteration taking $\varepsilon_r^{(n,k-1)}(x)$ as our solution. If neither of two conditions (2.24) is not reached at $n := N$, then we repeat the above sweep over the interval $[\underline{s}, \overline{s}]$ taking the pair $(q_N(x), V_N(x))$ as the new pair $(q_0(x), V_0(x))$. Usually at least one of conditions (2.24) is reached either on the third or on the fourth sweep, and the process stops then.

5

2.3. Computing functions $q_{n,k}(x), V_0(x)$**.** It seems to be at the first glance that for a given tail function $V_{n,k}(x)$, the function $q_{n,k}(x)$ can be computed as the solution of a conventional boundary value problem for Ordinary Differential Equation (2.20) with any two out of three boundary conditions (2.21). However, attempts to do so led to poor quality images, see Remark 3.1 in [14]. At the same time, the QRM has resulted in accurate solutions both in [14] and in Test 1 for synthetic data (below). The QRM is well designed to compute least squares solutions of PDEs with over-determined boundary conditions, such as, e.g. the problem (2.20), (2.21). We refer to the book [18] for the originating work about the QRM and to [7, 9, 13, 15, 16] for some follow up publications.

Let $L(q_{n,k})(x)$ and $P_{n,k}(x)$ be respectively left and right hand sides of (2.20). In our numerical studies $L(q_{n,k})(x)$ and $P_{n,k}(x)$ are written in the form of finite differences. Let $\alpha \in (0,1)$ be the regularization parameter. The QRM minimizes the following Tikhonov regularization functional

$$J_\alpha(q_{n,k}) = \|L_{n,k}(q_{n,k}) - P_{n,k}\|^2_{L_2(0,1)} + \alpha\|q_{n,k}\|^2_{H^2(0,1)}, \tag{2.25}$$

subject to boundary conditions (2.21). Here again norms in $L_2(0,1)$ and in the Sobolev space $H^2(0,1)$ are understood in the discrete sense. The functional $J_\alpha(q_{n,k})$ in (2.25) is quadratic. Using this fact as well as the tool of Carleman estimates, it can be shown that $J_\alpha(q_{n,k})$ has unique global minimum and no local minima [14, 15, 17]. We find that global minimum via the conjugate gradient method, minimizing with respect to the values of the function $q_{n,k}$ at grid points. We have used 100 grid points in the interval $(0,1)$. The step size in the $s-$direction was $h = 0.5$. The $s-$interval was $[\underline{s}, \overline{s}] = [3, 12]$. For each $n = 1, ..., N$ we take functions $q_{n,k}$ for $k = 1, ...m$ and we typically choose $m = 10$. The reason for the choice $m = 10$ is that numerical experience has shown that for each of the n tails stabilizes at $k \approx 10$. As to the regularization parameter α, we have found when testing synthetic data that $\alpha = 0.04$ is the optimal one, and we take it in our computations.

We now describe an important step of choosing the first tail function $V_0(x)$. To choose it, we consider the asymptotic behavior of the function $V(x, \overline{s})$ in (2.16) with respect to the truncation pseudo frequency $\overline{s} \to \infty$. This behavior is [14, 17]

$$V(x, \overline{s}) = \frac{p_0(x)}{\overline{s}} + O\left(\frac{1}{\overline{s}^2}\right), \ \overline{s} \to \infty.$$

We truncate the term $O(1/\overline{s}^2)$, which is somewhat similar with the defining of geometrical optics as a high frequency approximation of the solution of the Helmholtz equation. Hence, we take

$$V(x, \overline{s}) \approx \frac{p_0(x)}{\overline{s}}.$$

Since $q = \partial_s r$ and $V(x, \overline{s}) = r(x, \overline{s})$, then

$$q(x, \overline{s}) = -\frac{p_0(x)}{\overline{s}^2}. \tag{2.26}$$

Hence, setting in equation (2.17) $s := \overline{s}$ and using (2.26), we obtain the following *approximate* equation for the function $p_0(x)$

$$\frac{d^2}{dx^2}p_0(x) = 0, \ x \in (0,1). \tag{2.27}$$

Boundary conditions for $p_0(x)$ can be easily derived from (2.18) and (2.26) as

$$p_0(0) = -\overline{s}^2\psi_0(\overline{s}), \ p_0'(0) = -\overline{s}^2\psi_1(\overline{s}), \ p_0'(1) = 0. \tag{2.28}$$

We find an approximate solution $p_{0,appr}(x)$ of the problem (2.27), (2.28) via the QRM, similarly with the above. Next, we set for the first tail function

$$V_0(x) := \frac{p_{0,appr}(x)}{\overline{s}}. \tag{2.29}$$

A simplified formal statement of the global convergence theorem is the following (see Theorem 6.1 of [17] for more details and Theorem 6.7 of [7] for the 3d case).

Theorem 1. *Let the function $\varepsilon_r^*(x)$ be the exact solution of our CIP for the noiseless data $g^*(t)$ in (2.3). Fix the truncation pseudo frequency $\overline{s} > 1$. Let the first tail function $V_0(x)$ be defined via (2.27)-(2.29). Let $\sigma \in (0,1)$ be the level of the error in the boundary data, i.e.*

$$|\psi_0(s) - \psi_0^*(s)| \leq \sigma, \quad |\psi_1(s) - \psi_1^*(s)| \leq \sigma, \text{for } s \in [\underline{s}, \overline{s}],$$

where functions $\psi_0(s), \psi_1(s)$ depend on the function $g(t)$ in (2.3) via (2.7), (2.13), (2.18) and functions $\psi_0^*(s), \psi_1^*(s)$ depend on the noiseless data $g^*(t)$ in the same way. Let $h \in (0,1)$ be the grid step size in the $s-$direction in (2.19), let $\sqrt{\alpha} = \sigma$ and $\widetilde{h} = \max(\sigma, h)$. Let Q be the total number of functions $\varepsilon_r^{(n,k)}$ computed in the above algorithm. Then there exists a constant $D = D(x_0, d, \overline{s}) > 1$ such that if the numbers σ, h are so small that

$$\widetilde{h} < \frac{1}{D^{2Q+2}}, \tag{2.30}$$

then the following estimate is valid

$$\left\| \varepsilon_r^{(n,k)} - \varepsilon_r^* \right\|_{L_2(0,1)} \leq \widetilde{h}^{\omega}, \tag{2.31}$$

where the number $\omega \in (0,1)$ is independent on $n, k, \widetilde{h}, \varepsilon_r^{(n,k)}, \varepsilon_r^*$.

Therefore, Theorem 1 guarantees that if the total number Q of computed functions $\varepsilon_r^{(n,k)}$ is fixed and error parameters σ, h are sufficiently small, then obtained iterative solutions $\varepsilon_r^{(n,k)}(x)$ are sufficiently close to the exact solution ε_r^*, and this closedness is defined by the error parameters. Therefore the total number of iterations Q can be considered as the regularization parameter of our process, which is the additional regularization parameter to the number $\overline{s}$. The combination of inequalities (2.30) and (2.31) has a direct analog in the inequality of Lemma 6.2 on page 156 of the book [11] for classical Landweber iterations, which are defined for a substantially different ill-posed problem. As to the total number of iterations Q being a regularization parameter here, there is no surprise in this. Indeed, it is stated on page 157 of the book [11] that the number of iterations can serve as a regularization parameter for an ill-posed problem.

3. Imaging Results. The schematic diagram of the data collection by the forward looking radar is shown in Figure 3.1. Time resolved electromagnetic pulses are emitted by two sources installed on the radar. Only one component of the electric field is both transmitted and measured in the backscatter direction. The data are collected by sixteen detectors with the step size in time of 0.133 nanosecond. Data from shallow targets placed both below and above the ground were provided. The only piece of information provided by the ARL team (Sullivan and Nguyen) to Kuzhuget, Beilina, Klibanov and Fiddy was whether the target was located above the ground or was buried. The depth of the upper surface of a buried target was a few centimeters. GPS was used to provide the distance between the radar and a point on the ground located above that target to within a few centimeters error. The time resolved voltages induced by the backreflected signals were integrated over radar to target distances ranging from 8 to 20 meters and they were also averaged with respect to both source positions and with respect to the output of the sixteen detectors. Since we can assume here that the radar/target distance was known, then it was also approximately known which part of the measured time resolved signal would correspond to scattering events from that target, see Figure 3.1. Despite the presence of clutter, a single time dependent curve is extracted from the measured return time histories, as illustrated in Figure 3.1-(b). This is the form of the data that has been processed in each of the five measured data sets generated by ARL. A typical plot of returns without applying the inverse algorithm is shown in Figure 3.1-(c), where the triangle denotes a possible target of interest amongst the clutter from the backscatter generated from the volume of the region illuminated by the radar in Figure 3.1-(a). We process a set of averaged time histories like those shown in Figure 3.1-(b) to create a down range cut of the permittivity profile as indicated in Figure 3.1-(d).
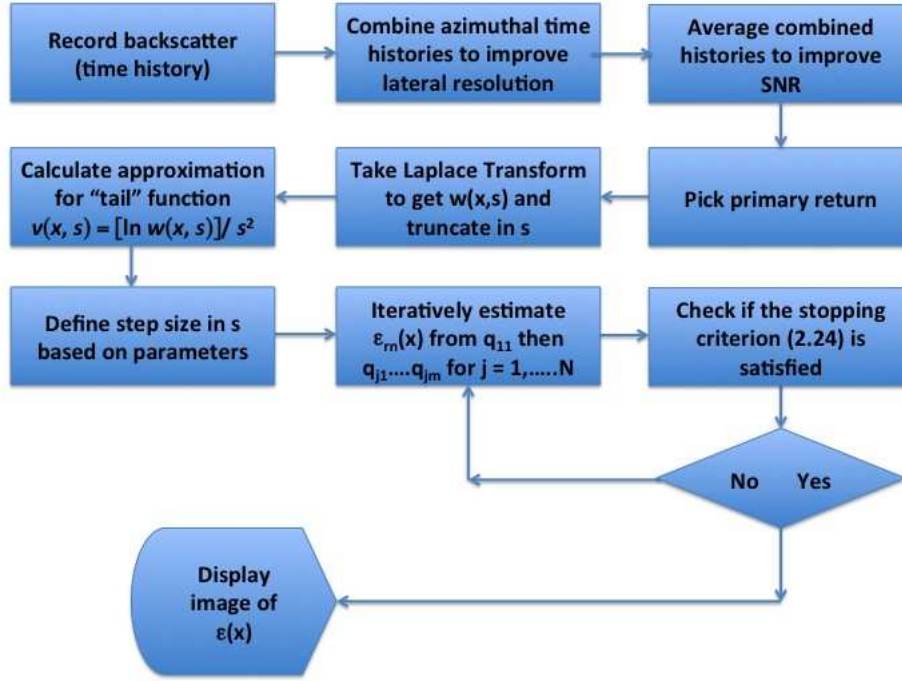
Fig. 2.1: *Flow chart of the algorithm.*

Our objective was to calculate ratios

$$R = \frac{\varepsilon_r \text{ (target)}}{\varepsilon_r \text{ (background)}} \tag{3.1}$$

of dielectric constants. If the ε_r (background) is known, then it is trivial to deduce ε_r (target). Clearly, for a target located above the ground, ε_r (background) = 1. In general we would expect the target volume to contain many inhomogeneities with a spatially varying $\varepsilon_r(x)$. A weighted average of dielectric constants of these constituent materials will be found over the volume spatial resolution cell that corresponds to the particular data acquisition configuration. In the examples presented here, we show results obtained from just one time history curve for each target, corresponding to one polarization component of the incident electromagnetic field and backscatter data measured and averaged over all sixteen receiver locations. Clearly this severely limits the transverse resolution but improves signal to noise ratio for 1d imaging in the propagation direction. The model is further simplified by using the 1d CIP employing only one hyperbolic partial differential equation. Consequently, the interpretation of the backscattering radiation will assign a high permittivity value to metal structures. Comparison between Figures 3.2-(a) and 3.2-(b) illustrates this. We use the upper bound ε_r (target) = 30 for the metallic targets because our calculations show that LT (2.7) from the response function $g(t)$ almost coincide for ε_r (target) ≥ 30.

In both cases of a metal structure and a high permittivity structure one can expect enhanced backscatter if the incident pulse includes frequencies that correspond to a normal mode of the target. Hence, we assign

$$10 \leq \varepsilon_r \text{ (metallic target)} \leq 30. \tag{3.2}$$

We call (3.2) *appearing dielectric constant of metallic targets.* In other words, we consider (3.2) *that regions appearing to have a high dielectric constant could also be metallic targets.*
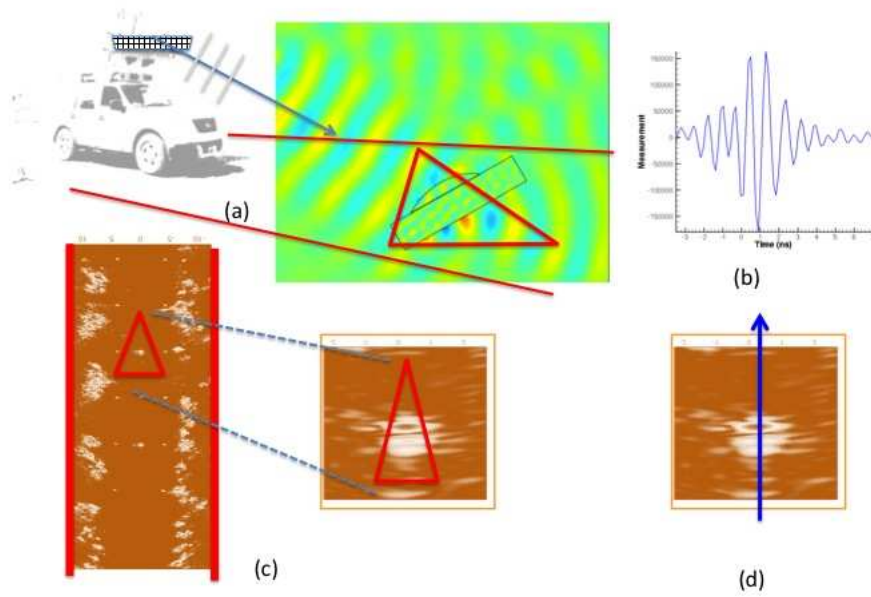
8

Fig. 3.1: *(a) a schematic diagram of the forward looking radar system illuminating a dielectric target; (b) a typical measured time history of the backscatter field; (c) a composite of unprocessed returns highlighting the dielectric target (indicated by the red triangle); (d) a down range cut of the permittivity profile which the new algorithm will generate.*
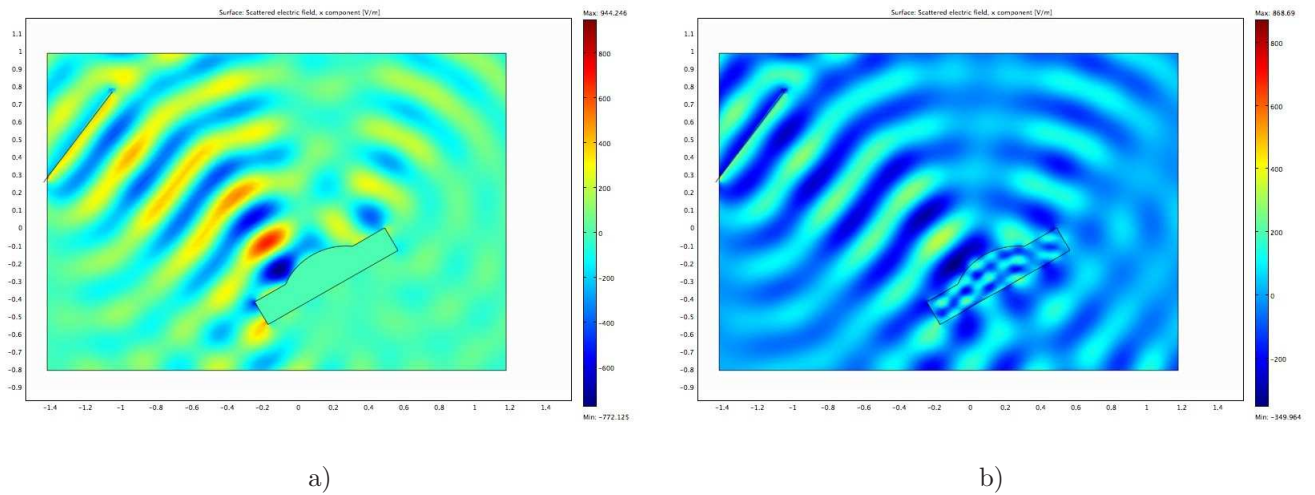

a)   b)

Fig. 3.2: *(a) scattered field from a metallic target, (b) scattered field from a high permittivity target with the same shape ($\varepsilon_r(\text{target}) = 10$); note the similarity between the backscatter electric fields in cases (a) and (b).*
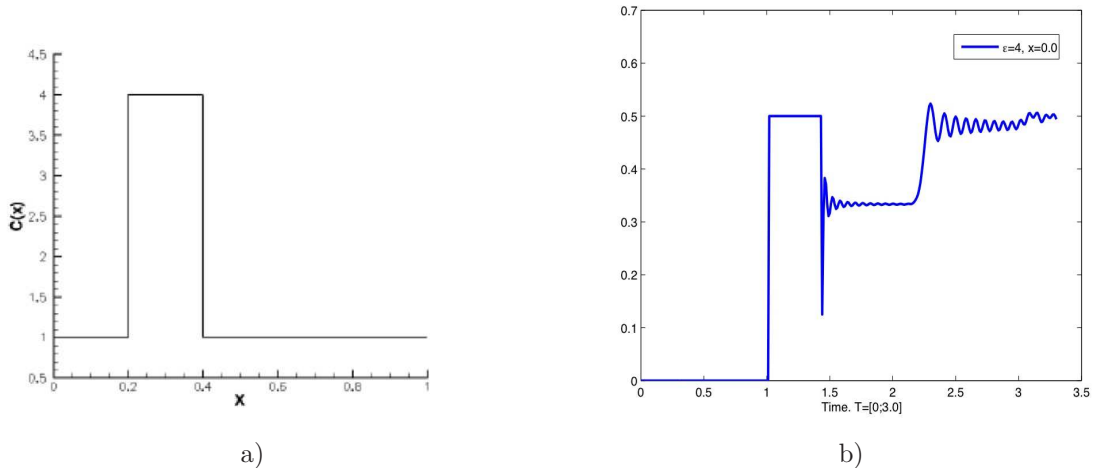
9

Fig. 3.3: *a) the function ε_r target) $= 4$, note that ε_r (background) $= 1$; b) $u(0,t) = g(t)$ for $0 < t < 3.0$. The source is located at $x_0 = -1$ and the first backscatter return is therefore seen at approximately $t = 2.4$ with "ringing" determined by interference of multiply scattered waves between the two boundaries of the block. Computations were performed using the software package WavES [23].*

To appreciate the kind of backscatter data and image recovery expected from a simple dielectric block, a 1d example illustrated below was investigated. Computations in this example were performed using the software package WavES [23]. The permittivity profile, ε_r (target) $= 4$, is shown in Figure 3.3-(a) and the computed function $u(0,t) = g(t)$ for $0 < t < 3$ in Figure 3.3-(b) (see in (2.3) for $g(t)$). We assume temporal units here for which at $t = 3$, a distance of $x = 3$ units is traversed and the source is at $x_0 = -1$ and the block's front face is at $x = 0.2$. Since the block is 0.2 units wide, $g(t)$ represents the backscatter return from the front and back face of the block. The reason why in Figure 3.3-(b) $g(t) = 0$ for $t < 1$ and $g(t) = 1/2$ for $1 \leq t \leq 1.4$ is that the solution of the problem (2.1), (2.2) for $\varepsilon_r(x) \equiv 1$ is $u_0(x,t) = H(t - |x - x_0|)/2$, where $H(z)$ is the Heaviside function,

$$H(z) = \left\{ \begin{array}{l} 0, z < 0, \\ 1, z \geq 0. \end{array} \right.$$

Hence, $u(0,t) = g(t) = H(t - 1)/2$ for $1 \leq t \leq 1.4$ and at $t = 1.4$ the return wave from the block hits the observation point $\{x = 0\}$ for the first time.

The measured data are also challenging to process since they arise from oblique illumination and the exact location and the amplitudes of the incident pulses were not known. Also, comparison of Figure 3.3-(b) with Figures 3.4-(b,d,f) shows that the measured data are highly oscillatory, unlike their simulated counterparts. Consequently, we applied an intuitively reasonable data pre-processing procedure, which remained totally unbiased since it was applied to blind data sets. The idea of this procedure is to make the data more similar to that shown in Figure 3.3-(b). Previously a similar procedure was reported for transmitted data in [6, 7, 12]. We have considered two cases:

Case 1. Suppose that the target is located above the ground. In this case

$$\varepsilon_r \text{ (target)} > \varepsilon_r \text{ (background)} = \varepsilon_r \text{ (air)} = 1. \tag{3.3}$$

Figures 3.3-(a,b) show that in this case the backscattering signal should be basically one downwards looking peak. Therefore, we have selected on the experimental curve the first downwards looking peak with the largest amplitude. As to the rest of the experimental curve, it was set to zero. Hence, we work only with the selected peak.
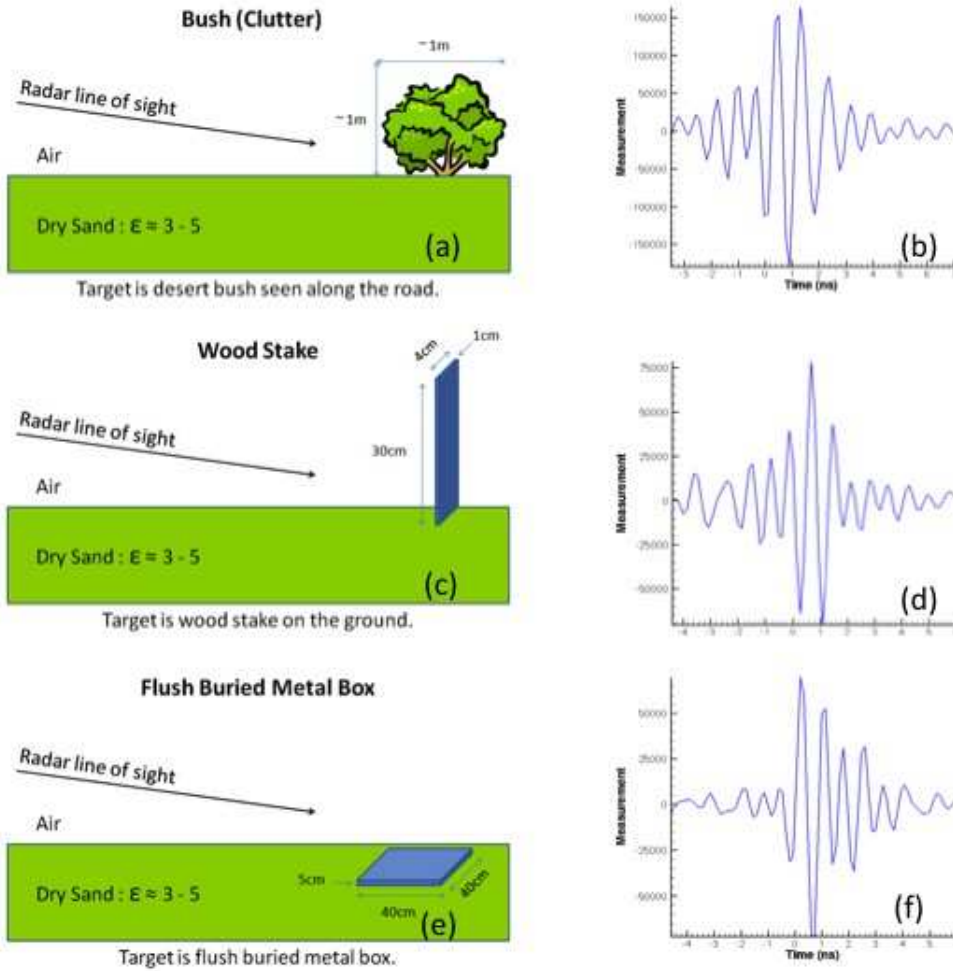
Fig. 3.4: *Three targets and their associated measured data. The ground is dry sand with $3 \leq \varepsilon_r \leq 5$ [21, 22]. The information shown in figures (a), (c) and (e) were only provided after computations were made. a) depicts a bush that was located on a road which generated background clutter; b) scaled experimental data for a) where the horizontal axis represents time in nanoseconds having a time step of 0.133 nanosecond and the vertical axis is the amplitude of the measured voltage at the detector; c) wooden stake and d) scaled experimental data for c); e) metal box buried in dry sand and f) scaled experimental data for e). The mismatch between experimental and simulated data (Figure 3.3-(b)) is evident.*

Case 2. Suppose that the target is buried in the ground. In this case we cannot claim the validity of (3.3). On the other hand, our numerical simulations (not shown here) have demonstrated that if ε_r (target) $<$ ε_r (background) , then in the analog of Figure 3.3-(b) the peak would look upwards. Therefore, in this case we have selected on the experimental curve the first peak with the largest amplitude to work with. As to the rest of the experimental curve, it was again set to zero.

We were provided with five data sets. Figure 3.5 shows superimposed pre-processed curves for all five targets we have worked with. The only peak which looks upwards, is the one for the plastic cylinder buried in soil, since its dielectric constant was less than the one of soil (see below). We stress once again that since Kuzhuget, Beilina, Klibanov and Fiddy have worked with blind data only, they did not know dielectric
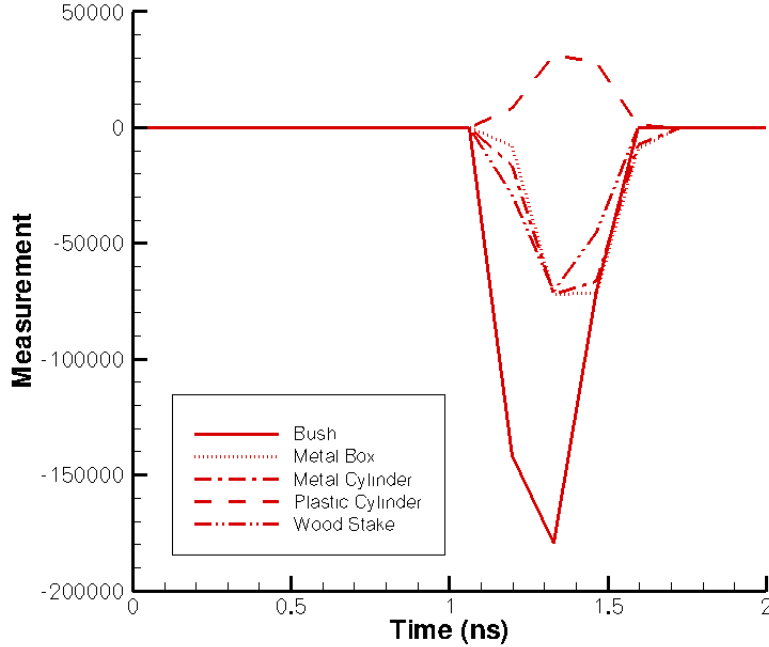
Fig. 3.5: *Superimposed pre-processed data for all five cases under consideration. The upward looking peak corresponds to the plastic cylinder; see Table 1.*

constants of targets in advance. Therefore, the choice of the upward looking peak in the case of the plastic cylinder was unbiased and was done only using the above rule. Note that the signals on Figure 3.5 are not yet multiplied by the scaling factor. Next, we have multiplied these data by the scaling factor 10^{-7}. This factor was chosen to have amplitudes of scaled signals to be similar with ones of simulated data from targets having dielectric constants ranging from ~2 to 40. For each set of experimental data, we have regarded the resulting curve as the function $u(0,t) - u_0(0,t) := g(t) - u_0(0,t)$. Next, we have worked only with this function as the data using the above algorithm. For simple isolated targets, these steps of data pre-processing are justified, given the accuracy of the results obtained upon *a posteriori* inspection. For more complex target volumes, a more sophisticated analysis of sets of time histories will be necessary.

The data sets were processed and the targets are illustrated in Figure 3.4. If we compare the highly oscillatory curves of Figures 3.4-(b), (d) and (f), one can see that these backscatter time histories or signatures are qualitatively quite similar in appearance. Their oscillatory nature is due to the specific carrier frequency and finite bandwidth of the pulsed radiation, while the simulated data assumes an idealized pulse. For these simple targets, we allow the above pre-processing step to force a correspondence between the two in order to identify the earliest return from the boundary of the target and determine its relative amplitude. Based on this, the inversion algorithm can determine a reliable estimate of that target's actual permittivity.

In addition to high oscillations of the data, we have faced two more uncertainties. First, we did not know where the time $t = 0$ is on our data. Second, we did not know where the actual location of the source x_0 is. This means that it is impossible to determine the location of the target. Hence, for computational purposes, we have arbitrarily assigned $t = 0$ to be a fixed location one (1) nanosecond off to the left from the beginning of the largest amplitude peak and $x_0 := -1$, knowing that we have independent GPS data to better fix absolute ranges should we need that information. Our primary objective here is to confirm the

quantitative accuracy of the estimates of the dielectric constant of each of the targets, i.e. to accurately image the ratio R in (3.1).

The derivative of the LT of the pre-processed data was computed for $0 < s < 12$ with a step size of $\Delta s = 0.05$. Since the calculation of the derivative of noisy data is an ill-posed problem, we have used the following well known formula for the calculation of the derivative of the LT

$$\varphi'(s) - \partial_s w_0(0, s) = -\int_0^\infty (g(t) - u_0(0, t)) t e^{-st} dt. \tag{3.4}$$

Since for all targets the function $g(t) - u_0(0, t) = 0$ for $t > 2$ (Figure 3.5), then integration in (3.4) is actually carried for $0 < t < 2$. We then define boundary conditions for functions $q_{n,k}$ for each n, and R is calculated by the above algorithm.

In Figures 3-(a)-(f) we regard R as the maximal amplitude of the calculated peak. We first verified that the algorithm provides a good estimate for R using simulated data. For the block in Figure 3.3-(a) we obtain the 1a image shown in Figure 3-(a) which was found $\varepsilon_r = 3.8$ which is very close to the known value of 4. Next, we have calculated images from experimental data. In addition to Figures 3.4-(a,c,e), we have also imaged two more cases: a plastic cylinder and a metal cylinder, both buried in the ground with schematic diagrams similar with the one on Figure 3.4-(e). Figures 3-(b)-(f) display our calculated images for all five targets.

Dielectric constants were not measured when the data were collected. Therefore, we have compared computed values of dielectric constants with those listed in Tables [21, 22]. Note that these tables often provide a range of values rather than exact numbers, but given this caveat, the calculated results for these materials are well within the range of expectations, see Table 1 below.

Table 3.1: *Computed values for R, the relative dielectric constant in (3.1), based on blind processing of measured backscatter data from five different targets. Here A means air and B means dry sand.*

Target	A/B	R	ε_r (backgr)	ε_r (target), calc.	ε_r (target), published.
Figure 3.3-(a)	n/a	3.8	1	3.8	4 (known)
Bush	A	6.5	1	6.5	3 to 20 [10]
Wood stake	A	3.8	1	3.8	2 to 6 [21]
Metal box	B	3.8	3 to 5 [21]	11.4 to 19	10 to 30 (3.2)
Metal cylinder	B	4.3	3 to 5 [21]	12.9 to 21.4	10 to 30 (3.2)
Plastic cylinder	B	0.4	3 to 5 [21]	1.2 to 2	1.1 to 3.2 [21, 22]

4. Conclusions. We have described a new method for recovering quantitatively reliable estimates of target's material properties (dielectric constants) from backscatter field measurements. The method is an inverse scattering algorithm based on a rigorously formulated Coefficient Inverse Problem. The numerical method is constructed to ensure global convergence and therefore avoids stagnation at erroneous solutions for images of target permittivity distributions. Furthermore, the method requires no prior knowledge of the inhomogeneities present in the target volume. These properties are rigorously guaranteed. The authors are unaware about numerical method with similar features for the case of Coefficient Inverse Problems with single measurement data.

The approach was evaluated here using data provided by ARL from a forward looking radar system without prior knowledge of the targets being used. The data were measured using oblique incidence and with unknown source locations, and so some assumptions were made to provide the necessary inputs for the algorithm. The procedure first estimates a solution that has defined error given the quality of the data but which is guaranteed to be reliable. To simplify matters, only images of dielectric constants were recovered in order to validate the quantitative accuracy of the approach. Data sets were pre-processed and a downrange 1d permittivity profile calculated. Additional work needs to be done to extend the algorithm to make use
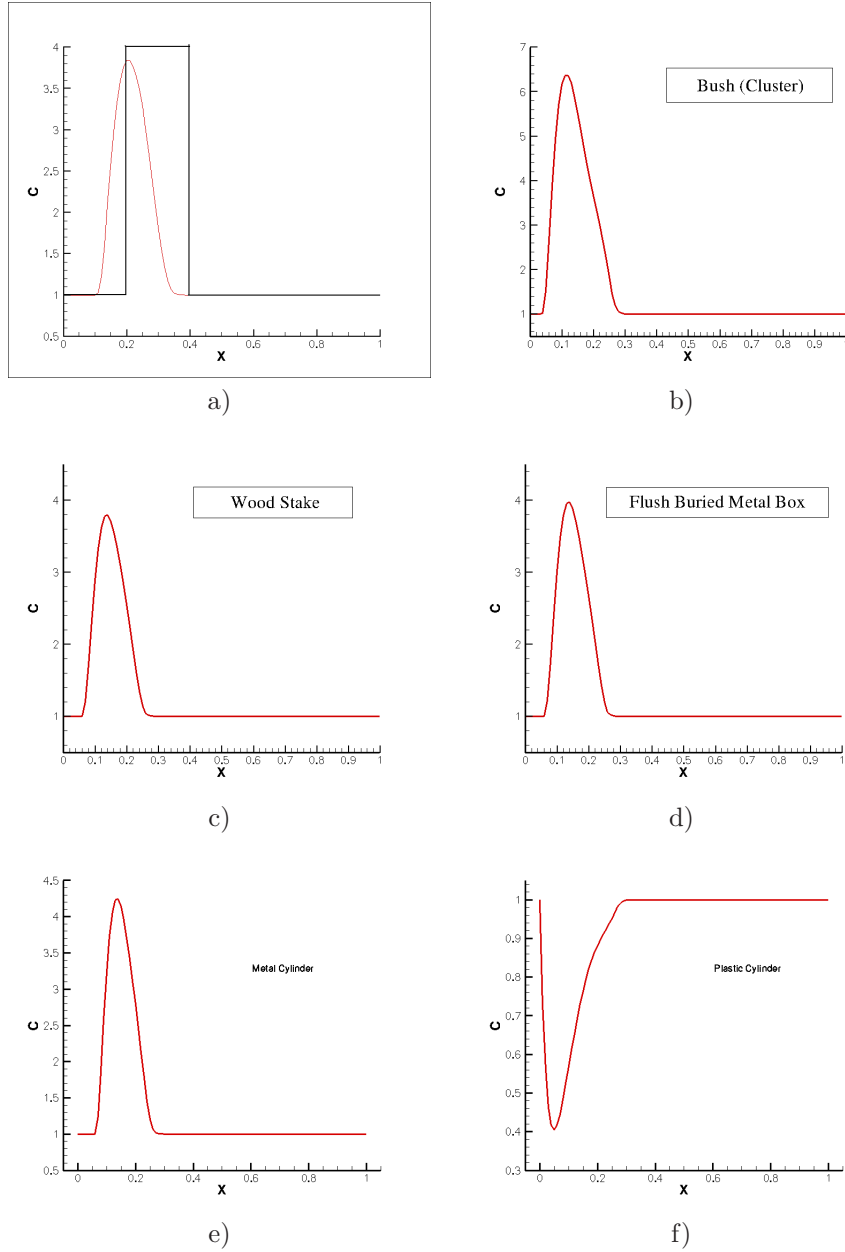
a) b)

c) d)

e) f)

Fig. 3.6: *Calculated images of targets. The ratio R in (3.1) is regarded as the maximal amplitude of the imaged peak. a) The image for computationally simulated data as a verification of the accuracy of our algorithm. Rectangular block and the curve are respectively true and computed profiles of the dielectric constant. The computed target/background contrast $R = 3.8$, which corresponds to a 5% of error. b) The image of the bush, see Figure 3.1-(a). The calculated ε_r(bush)=6.5, which is in the range of tabulated values $3 \leq \varepsilon_r \leq 20$ [10]. c) the image of the wood stake, see Figure 3.3-(c). The calculated ε_r (wood stake)=3.8 [10]. d) The image of the buried metal box, see Figure 3.4-(e). The calculated $R = 3.8$. Since the background was dry sand with $3 \leq \varepsilon_r$(dry sand)≤ 5 [21], then the calculated ε_r(metal box) is between 11.4 and 19. This is within the range (3.2) of appearing dielectric constants of metallic targets. e) The calculated image of buried metal cylinder. The calculated ratio $R = 4.3$. Similarly with d) we conclude that the calculated value of ε_r(metal cylinder) is between 12.9 and 21.4. This is again within the range (3.2) of appearing dielectric constants of metallic targets. f) The calculated image of buried plastic cylinder. The calculated ratio $R = 0.4$. Similarly with d) we conclude that the calculated value of the dielectric constant is ε_r(plastic cylinder) is between 1.2 and 2.5, which is again within the range of tabulated values for plastic [21, 22].*

14

of the angular spread of backscatter time histories to validate the eventual 3d spatial resolution achievable from a single point data of interest here.

Since dielectric constants were not measured in the ARL experiments, then the maximum one can achieve is to compare computational results with tabulated values. Table 1 shows the computed relative permittivities of targets without any prior knowledge whatsoever of those targets. It is clearly seen that all fall well within expected tabulated limits for the materials in question. We emphasize that these results were obtained despite severely limited information content, large noise in the data and significant discrepancies between experimental and simulated data. We can conclude therefore that these results point towards both the validity of our mathematical model and the highly robust nature of the numerical algorithm.

Acknowledgments

REFERENCES

[1] L. Beilina and C. Johnson, A hybrid FEM/FDM method for an inverse scattering problem. In *Numerical Mathematics and Advanced Applications - ENUMATH 2001*, Springer-Verlag, 2001.

[2] L. Beilina and C. Johnson, A posteriori error estimation in computational inverse scattering, *Mathematical Models and Methods in Applied Sciences*, 15, 23-37, 2005.

[3] L. Beilina and M.V. Klibanov, A globally convergent numerical method for a coefficient inverse problem *SIAM J. Sci. Comp.*, 31, 478-509, 2008.

[4] L. Beilina and M.V. Klibanov, *A posteriori* error estimates for the adaptivity technique for the Tikhonov functional and global convergence for a coefficient inverse problem *Inverse Problems,* 26, 045012, 2010.

[5] L. Beilina and M.V. Klibanov and M.Yu. Kokurin, Adaptivity with relaxation for ill-posed problems and global convergence for a coefficient inverse problem, *J. of Mathematical Sciences,* 167, 279-325, 2010.

[6] L. Beilina and M.V. Klibanov, Reconstruction of dielectrics from experimental data via a hybrid globally convergent/adaptive algorithm, *Inverse Problems,* 26, 125009, 2010.

[7] L. Beilina and M.V. Klibanov, *Approximate Global Convergence and Adaptivity for Coefficient Inverse Problems* Springer, New York, 2012.

[8] L. Beilina and M.V. Klibanov, The philosophy of the approximate global convergence for multidimensional coefficient inverse problems *Complex Variables and Elliptic Equations*, accepted for publication.

[9] H. Cao, M.V. Klibanov and S.V. Pereverzev, A Carleman estimate and the balancing principle in the quasi-reversibility method for solving the Cauchy problem for the Laplace equation, *Inverse Problems,* 25, 35005, 2009.

[10] H.T. Chuah, K.Y. Lee and T.W. Lau, Dielectric constants of rubber and oil palm leaf samples at X-band, *IEEE Trans. on Geoscience and Remote Sensing,* 33, 221-223, 1995.

[11] H.W. Engl, M. Hanke and A. Neubauer, *Regularization of Inverse Problems*, Kluwer Academic Publishers, Boston, 2000.

[12] M.V. Klibanov, M.A. Fiddy, L. Beilina, N. Pantong and J. Schenk, Picosecond scale experimental verification of a globally convergent numerical method for a coefficient inverse problem, *Inverse Problems,* 26, 045003, 2010.

[13] M.V. Klibanov and A. Timonov, *Carleman Estimates for Coefficient Inverse Problems and Numerical Applications*, VSP, Utrecht, The Netherlands, 2004.

[14] A.V. Kuzhuget and M.V. Klibanov, Global convergence for a 1-D inverse problem with application to imaging of land mines, *Applicable Analysis,* 89, 125-157, 2010.

[15] A.V. Kuzhuget, N. Pantong and M.V. Klibanov, A globally convergent numerical method for a Coefficient Inverse Problem with backscattering data, *Methods and Applications of Analysis,* 18, 47-68, 2011.

[16] A.V. Kuzhuget, L. Beilina and M.V. Klibanov, Approximate global convergence and quasi-reversibility for a coefficient inverse problem with backscattering data, *J. of Mathematical Sciences*, 181, 19-49, 2012.

[17] A.V. Kuzhuget, L. Beilina, M.V. Klibanov, A. Sullivan, L. Nguyen and M.A. Fiddy, Blind experimental data collected in the field and and approximately globally convergent inverse algorithm, preprint available online at http://www.ma.utexas.edu/mp_arc/.

[18] R. Lattes R and J.-L. Lions, *The Method of Quasireversibility: Applications to Partial Differential Equations,* Elsevier, New York, 1969.

[19] L. Nguyen, D. Wong, M. Ressler, F. Koenig, B. Stanton, G. Smith, J. Sichina and K. Kappra, Obstacle avoidance and concealed target detection using the Army Research Lab ultra-wideband synchronous impulse Reconstruction (UWB SIRE) forward imaging radar *Proc. SPIE,* 6553, 65530H (1)-65530H (8), 2007.

[20] P.M. van den Berg, Modified gradient and contrast source inversion, Chapter 2 of "*Analytical and Computational*

Methods in Scattering and Applied Mathematics", edited by F. Santosa and I Stakgold, Chapman and Hall- CRC, 2000.

[21] Tables of dielectric constants at http://www.asiinstr.com/technical/Dielectric_Constants.htm.

[22] Tables of dielectric constants at http://www.krohne.com/Dielectric_Constants.6840.0.html.

[23] Software package Wave Equations Solutions at http://www.waves24.com/